Supplementary Information for Seismic Evidence for Increasing Unfrozen Pore Water Heterogeneity from Roadside to Coastal Arctic Tundra

Guilherme Zakarewicz[1], Gabriel Rocha dos Santos[1], Eileen R. Martin[2], Ming Xiao[3], and Tieyuan Zhu[1]

[1]Department of Geosciences, The Pennsylvania State University, University Park, PA, USA
[2]Department of Geophysics, Department of Applied Math and Statistics, Colorado School of Mines, Golden, CO, USA
[3]Department of Civil and Environmental Engineering, The Pennsylvania State University, State College, PA, USA

Correspondence: Tieyuan Zhu (tyzhu@psu.edu)

S1 DAS, geophone, and MASW processing details

We analyzed two independent active-source MASW datasets acquired at the same five study sites. The DAS survey was collected in August 2024 along the buried fiber-optic cable using a Terra15 interrogator. The DAS data were recorded as strain-rate measurements with 2.45 m channel spacing, 5 m gauge length, and 1000 Hz sampling. The conventional geophone survey was acquired in August 2022 using a linear array of 22 vertical-component geophones with 1 m spacing and 4000 Hz sampling (Table S1). In both surveys, seismic energy was generated using sledgehammer impacts. Both surveys targeted the same locations, but they are not exactly co-located. Instead, they have a short lateral offset ranging from 5–45 m, reported in Table S4, and the local acquisition geometry for each site is shown in Figure S1.

For both datasets, we applied multichannel analysis of surface waves (MASW) to estimate 1D V_s profiles from surface-waves dispersion (Park et al., 1998, 1999). The records were detrended, demeaned, and bandpass filtered prior to dispersion analysis. DAS records were additionally downsampled to 500 Hz before processing. Dispersion images were computed using the phase-shift method (Park et al., 1998), and the fundamental-mode dispersion curves were manually picked from the frequency–phase velocity (f–v) images. The picked dispersion curves were inverted using the *Dinver* package in *Geopsy*. The inversion uses the Neighborhood Algorithm, a stochastic search method that samples candidate velocity models and evaluates their misfit relative to the observed dispersion curve. For each shot, we retained the ensemble of the 1000 best-fitting models. The median of this ensemble was used as the representative V_s profile, and the model distribution was used to define uncertainty bounds shown in the main text. These DAS- and geophone-derived V_s profiles provide the seismic input for the rock-physics interpretation.

S2 Survey geometry at the five comparison sites

Figure S1 shows the acquisition geometry for the five DAS–geophone comparison sites. The panels illustrate the DAS cable segment used for MASW processing and the corresponding geophone array at each location, highlighting that the paired profiles are separated by short lateral offsets rather than being exactly co-located.

S3 Load-bearing rock-physics model

We used the load-bearing effective-medium model (Helgerud et al., 1999; Mavko et al., 1998; Dvorkin and Nur, 1996; Dou et al., 2017) to relate V_s to the ice/water content in partially frozen sediment. In this model, pore ice is treated as part of the load-bearing solid frame rather than as a pore fluid. Therefore, increasing ice saturation reduces the pore volume available to liquid water and modifies the elastic properties of the effective solid phase.

The main text defines the initial or thaw-state porosity ϕ_0, ice saturation S_i, water saturation $S_w = 1 - S_i$, and the effective porosity available to liquid water:

$$\phi(S_i) = \phi_0(1 - S_i) = \phi_0 S_w. \tag{S1}$$

The volumetric fractions of mineral, ice, and liquid water are

$$V_m = 1 - \phi_0, \qquad V_i = \phi_0 S_i, \qquad V_f = \phi_0(1 - S_i). \tag{S2}$$

The initial porosity ϕ_0 and the effective fluid-filled porosity $\phi(S_i)$ should not be confused with the critical porosity ϕ_c. The critical porosity is a fixed Hertz–Mindlin parameter, whereas ϕ_0 is allowed to vary with depth during the porosity inversion.

The effective solid phase is represented as a mineral–ice mixture. The ice and mineral fractions within the solid phase are

$$f_i = \frac{V_i}{V_m + V_i}, \qquad f_m = 1 - f_i. \tag{S3}$$

The Voigt bounds for the bulk and shear moduli of the effective solid phase are

$$K_s^{\mathrm{V}} = f_m K_m + f_i K_i, \qquad G_s^{\mathrm{V}} = f_m G_m + f_i G_i, \tag{S4}$$

where K_m and G_m are the mineral bulk and shear moduli, and K_i and G_i are the corresponding ice moduli. The Reuss bounds are

$$K_s^{\mathrm{R}} = \left(\frac{f_m}{K_m} + \frac{f_i}{K_i}\right)^{-1}, \qquad G_s^{\mathrm{R}} = \left(\frac{f_m}{G_m} + \frac{f_i}{G_i}\right)^{-1}. \tag{S5}$$

The Voigt–Reuss–Hill averages are then

$$K_s = \frac{K_s^{\mathrm{V}} + K_s^{\mathrm{R}}}{2}, \qquad G_s = \frac{G_s^{\mathrm{V}} + G_s^{\mathrm{R}}}{2}. \tag{S6}$$

The Poisson's ratio of the effective mineral–ice solid phase is calculated as

$$\nu_s = \frac{3K_s - 2G_s}{2(3K_s + G_s)}. \tag{S7}$$

The Hertz–Mindlin bulk and shear moduli at critical porosity are

$$K_{\mathrm{HM}} = \left[\frac{n^2(1-\phi_c)^2 G_s^2 P}{18\pi^2(1-\nu_s)^2}\right]^{1/3}, \tag{S8}$$

and

$$G_{\mathrm{HM}} = \frac{5-4\nu_s}{5(2-\nu_s)}\left[\frac{3n^2(1-\phi_c)^2 G_s^2 P}{2\pi^2(1-\nu_s)^2}\right]^{1/3}, \tag{S9}$$

where n is the coordination number, P is the effective pressure, and ϕ_c is the critical porosity. The fixed values used in this study are listed in Table S2.

The dry-frame moduli at the effective porosity $\phi = \phi(S_i)$ are calculated using a modified Hashin–Shtrikman lower-bound interpolation. The dry-frame bulk modulus is

$$K_{\mathrm{dry}} = \left[\frac{\phi/\phi_c}{K_{\mathrm{HM}} + \frac{4}{3}G_{\mathrm{HM}}} + \frac{1-\phi/\phi_c}{K_s + \frac{4}{3}G_{\mathrm{HM}}}\right]^{-1} - \frac{4}{3}G_{\mathrm{HM}}. \tag{S10}$$

For the shear modulus, we first define

$$\zeta_{\mathrm{HM}} = \frac{G_{\mathrm{HM}}}{6}\left(\frac{9K_{\mathrm{HM}} + 8G_{\mathrm{HM}}}{K_{\mathrm{HM}} + 2G_{\mathrm{HM}}}\right). \tag{S11}$$

The dry-frame shear modulus is then

$$G_{\mathrm{dry}} = \left[\frac{\phi/\phi_c}{G_{\mathrm{HM}} + \zeta_{\mathrm{HM}}} + \frac{1-\phi/\phi_c}{G_s + \zeta_{\mathrm{HM}}}\right]^{-1} - \zeta_{\mathrm{HM}}. \tag{S12}$$

Gassmann fluid substitution is used to calculate the saturated bulk modulus:

$$K_{\mathrm{sat}} = K_{\mathrm{dry}} + \frac{\left(1 - \frac{K_{\mathrm{dry}}}{K_s}\right)^2}{\frac{\phi}{K_f} + \frac{1-\phi}{K_s} - \frac{K_{\mathrm{dry}}}{K_s^2}}. \tag{S13}$$

Gassmann substitution does not modify the shear modulus:

$$G_{\mathrm{sat}} = G_{\mathrm{dry}}. \tag{S14}$$

Although K_{sat} does not enter directly into the calculation of V_s, it is included here for completeness. The bulk density is

$$\rho_{\mathrm{bulk}} = V_m \rho_m + V_i \rho_i + V_f \rho_f, \tag{S15}$$

where ρ_m, ρ_i, and ρ_f are the mineral, ice, and liquid-water densities. The predicted shear-wave velocity is

$$V_s = \sqrt{\frac{G_{\mathrm{sat}}}{\rho_{\mathrm{bulk}}}}. \tag{S16}$$

For a prescribed initial porosity ϕ_0, these equations define a monotonic relationship between V_s and S_w. This relationship is inverted numerically to map the MASW-derived velocity profiles into physically plausible water-saturation profiles.

S4 Site-specific joint porosity inversion

The conversion from V_s to S_w is nonunique because the same shear-wave velocity can be reproduced by different combinations of porosity and ice/water saturation. To reduce this nonuniqueness, we first performed a site-specific joint inversion to estimate a depth-dependent porosity profile for each DAS–geophone pair. This step was used to obtain physically plausible porosity profiles that allow both seismic profiles at a given site to be mapped into water saturation while remaining consistent with the temperature-derived reference profile.

For each site, we used the median V_s profiles from the DAS and geophone MASW inversions. The profiles were discretized on a 1 m depth grid and truncated at 40 m depth. The temperature-derived reference S_w profile was interpolated onto the same depth grid using a shape-preserving PCHIP interpolation. Only depths where the temperature-derived median profile was finite were included in the inversion.

For a given porosity value ϕ_0, the load-bearing model provides a monotonic relationship between ice saturation S_i and predicted V_s. We inverted this relationship by interpolation to estimate S_i from the observed V_s values, and then computed

$$S_w = 1 - S_i.$$

This mapping was repeated over a porosity grid from $\phi_0 = 0.05$ to $\phi_0 = 0.95$, producing lookup libraries $S_w^{\mathrm{geo}}(z, \phi_0)$ and $S_w^{\mathrm{DAS}}(z, \phi_0)$ for the geophone and DAS median profiles, respectively.

For each site, we then solved for a single depth-dependent porosity profile $\phi_0(z)$ shared by the DAS and geophone profiles. The objective function was

$$
\begin{aligned}
J(\phi_0) = & \sum_z w_{\mathrm{geo}} \left[S_w^{\mathrm{geo}}(z, \phi_0(z)) - S_w^{\mathrm{ref}}(z)\right]^2 \\
& + \sum_z w_{\mathrm{DAS}} \left[S_w^{\mathrm{DAS}}(z, \phi_0(z)) - S_w^{\mathrm{ref}}(z)\right]^2 \\
& + \lambda \sum_z \left(\frac{d\phi_0}{dz}\right)^2 \\
& + \mu \sum_z \left[\phi_0(z) - \phi_{\mathrm{prior}}(z)\right]^2 .
\end{aligned}
$$

where S_w^{ref} is the temperature- and laboratory-derived median S_w profile. The first two terms force the DAS- and geophone-derived S_w profiles to remain consistent with the reference. The third term imposes vertical smoothness on the porosity profile, and the fourth term penalizes deviations from a prescribed porosity prior.

The porosity prior was defined as

$$
\phi_{\mathrm{prior}}(z) = \phi_{\mathrm{deep}} + \frac{\phi_{\mathrm{surface}} - \phi_{\mathrm{deep}}}{1 + (z/z_c)^p},
$$

with $\phi_{\mathrm{surface}} = 0.90$, $\phi_{\mathrm{deep}} = 0.22$, $z_c = 2.0$ m, and $p = 3.0$. The inversion used $\lambda = 2.0$, $\mu = 0.1$, and equal weights for the geophone and DAS terms. Optimization was performed with the L-BFGS-B algorithm using bounds $0.05 \leq \phi_0 \leq 0.95$ at each depth sample.

This joint inversion does not imply that the recovered porosity profile is unique. Instead, it provides a regularized porosity profile that prevents the DAS–geophone velocity differences from being explained by arbitrary and independent porosity variations. The two seismic profiles at each site are allowed to produce different S_w profiles, but they are required to share the same porosity structure.

S5 Global porosity reference and final S_w mapping

After the site-specific joint inversion, we obtained one optimized porosity profile $\phi_0^{(j)}(z)$ for each of the five study locations. These profiles were not used directly as the final porosity profiles for each site. Instead, we combined them to define a common porosity reference for the full transect. The global mean porosity profile was calculated as

$$
\bar{\phi}_0(z) = \frac{1}{N} \sum_{j=1}^{N} \phi_0^{(j)}(z),
$$

where $N = 5$ is the number of sites. We also computed the 10th and 90th percentiles of the five porosity profiles at each depth to represent the range of porosity models obtained from the joint inversion. The resulting global porosity reference is shown in Figure S2.

The final S_w profiles shown in the main text were then obtained in a forward-mapping step using this global mean porosity profile. For each site and acquisition type, we rebuilt the V_s–S_w lookup library from the median MASW-derived V_s profile and applied the same depth-dependent porosity profile $\bar{\phi}_0(z)$. This produced the final geophone- and DAS-derived water saturation profiles,

$$S_w^{\mathrm{GEO}}(z) = F\left[V_s^{\mathrm{GEO}}(z), \bar{\phi}_0(z)\right],$$

$$S_w^{\mathrm{DAS}}(z) = F\left[V_s^{\mathrm{DAS}}(z), \bar{\phi}_0(z)\right],$$

where F denotes the inverse lookup operation based on the load-bearing rock-physics model.

To evaluate the sensitivity of the final S_w estimates to the porosity reference, we repeated the forward mapping using the global p10 and p90 porosity profiles. The resulting S_w profiles define a porosity-related uncertainty band. Because the ordering of S_w obtained from the p10 and p90 porosity profiles is not necessarily fixed at all depths, the lower and upper bounds were defined as the minimum and maximum values from the two mappings at each depth.

This final mapping step ensures that all DAS and geophone profiles are interpreted using the same porosity reference. Therefore, the differences between paired DAS- and geophone-derived S_w profiles primarily reflect differences in the observed V_s structure rather than arbitrary site-specific porosity choices. The site-specific porosity inversions are used only to define a physically plausible common porosity reference and its uncertainty range.

The final use of a global mean porosity profile follows the same regularization principle. We assume that the dominant short-offset differences between paired DAS and geophone profiles are more likely to reflect variations in permafrost phase state than completely independent changes in porosity structure. Using a common porosity reference therefore provides a conservative framework for comparing S_w between sites and acquisition types. If each profile were allowed to use an independent porosity model, part of the observed velocity contrast could be absorbed by porosity variations, leading to smaller and less physically constrained S_w differences.

The shaded regions around the final S_w profiles were obtained by repeating the V_s–S_w mapping using the global p10 and p90 porosity profiles. These bands represent a porosity-related sensitivity range, not a formal uncertainty estimate.

To quantify the differences between the paired DAS- and geophone-derived S_w profiles, we calculated the mean absolute difference, root-mean-square difference, maximum absolute difference, and mean signed difference at each site (Table S5). The metrics were calculated over the full modeled depth interval from 0 to 40 m. We define the signed difference as

$$\Delta S_w(z) = S_{w,\mathrm{DAS}}(z) - S_{w,\mathrm{Geo}}(z).$$

Positive values therefore indicate higher inferred S_w in the DAS-derived profile. The results provide a quantitative measure of the short-offset phase-state contrasts shown in the main text.

S6 Comparison with alternative V_s-S_w rock-physics models

To justify the selection of the load-bearing effective-medium model over alternative formulations, we compared its predicted S_w against four additional published models: the two-end-member mixing model of Dou et al. (2017), Zimmerman and King (1986), Minshull (1994), and Carcione (1998). For this comparison only, all models were evaluated using a constant porosity of 0.4, independent of the depth-dependent porosity profile used in the main V_s-S_w workflow, so that differences between curves reflect the choice of rock-physics formulation rather than porosity. Each model was applied to the median DAS V_s profile at five sites (Roadside, Tundra 1, Tundra 2, Tundra 3, Tundra 4) and compared against the reference profile (Section 3.1; Figure S3). Two models (load-bearing model and Carcione 1998) track the reference closely and remain largely within its p10–p90 envelope, whereas the other three depart sharply and predict physically implausible unfrozen water content by 10–20 m. Carcione (1998) predicts $S_w = 0$ for almost all sites at deep portions, which contradicts the physical expectation that interfacial liquid water persists at subzero temperatures (Section 3.4), therefore keeping some fraction of unfrozen pore water content. The one exception is Tundra 4, where Carcione (1998) tracks the reference at least as closely as the load-bearing model and does not decay to $S_w = 0$ at depth. We nonetheless retain the load-bearing model at this site, consistent with the rest of the transect, so that the reference-relative anomalies reported in the main text are derived from a single rock-physics formulation applied uniformly across all five sites rather than a model chosen independently at each location.

S7 Robustness to common vs site-specific reference profiles

In the main workflow, the reference profile pools the fitted freezing curves from all 12 permafrost core samples of Wang et al. (2025), constructing a single reference profile shared by all sites during the analysis. To evaluate whether this approach could affect real site-to-site variability in the reference itself, we repeated the full workflow using site-specific reference profiles built only from the samples collected near each site's corresponding borehole, i.e. boreholes S1-S5 from Wang et al. (2025). Tundra 1, Tundra 2, and Tundra 3 had 2, 4, and 5 nearby samples, respectively; Tundra 4 had only one sample, so no percentile range could be computed and its reference envelope collapses to the median. Roadside had no samples of its own, so we used the Tundra 1 reference as the nearest available substitute. Each site-specific reference was evaluated at the local temperature profile following the same procedure as the common reference.

We then repeated the joint DAS–geophone porosity inversion independently at each site, using identical regularization, priors, and optimization settings as the main pipeline, but evaluating each site's objective function against its own site-specific reference rather than the common one. The five resulting site-specific porosity profiles were averaged into a new global porosity profile following the same procedure as the main workflow, and used in an independent forward V_s–S_w mapping to obtain site-specific S_w profiles for both DAS and geophone. The site-specific and pooled-reference pipelines produce closely similar S_w profiles at all five sites (Figure S4). Both the DAS–geophone contrast and the RMS relative to the reference (Table S3) show the same site-dependent pattern under either pipeline (increasing from Roadside toward Tundra 4) indicating that the spatial pattern reported in the main text is present both using a common reference and using site-specific references.

S8 Quantitative comparison of DAS- and geophone-derived V_s profiles

To complement the site comparisons discussed in the main text, we calculated additional quantitative metrics between DAS and geophone median V_s profiles at each location considering 0-40 m depth (Table S4). Also, Figures S5 and S6 show the depth-dependent differences between the DAS- and geophone-derived median V_s profiles at each site. For each site, we plot (i) the inversion results for DAS and geophone systems, including the median and uncertainty bounds; (ii) the absolute velocity difference as a function of depth, (iii) the absolute percentage error, and (iv) a point-by-point V_s scatter comparison.

S9 Effect of lateral offset on dispersion curves within a single sensor

To assess whether the observed DAS–geophone differences could arise simply from comparing two different sensing systems rather than from real subsurface variability, we tested whether lateral offset alone produces measurable differences in dispersion curves by using data from a single sensor. We used data from a single shot acquired in the Roadside portion of the DAS cable and split the shot gather into left and right halves, each containing approximately half the total channel range. Then, we processed each half independently applying the same MASW workflow. The resulting dispersion images and picked curves differ measurably between both sides (Figure S7), consistent with each half sensing a laterally offset subsurface structure. This indicates that lateral offset by itself can produce dispersion curve differences, independent of any difference in sensing technology. This supports the interpretation that the differences observed in the main results reflect primarily real subsurface structure rather than artifacts of comparing two different sensing systems.

S10 Sensitivity kernel analysis of the MASW dispersion curves

To evaluate the depth range independently constrained by each dispersion curve, we computed the sensitivity of the fundamental-mode Rayleigh-wave phase velocity to shear-wave velocity, $\partial c/\partial V_s(z)$, for the median DAS and geophone Vs profile at each site (Figure S8). Sensitivity kernels were calculated using the PhaseSensitivity module of the disba Python package (Luu, 2021). The procedure was applied independently to the DAS- and geophone-derived median Vs profile at each site, evaluated over each dataset's own minimum reliably picked frequency (fmin; Table S8), since fmin varies between sites and sensing systems and controls the longest wavelength (and therefore the greatest depth) sampled by the dispersion curve.

For each site and sensor, we defined the resolution depth as the depth at which the frequency-integrated sensitivity decays to 10% of its peak value. This threshold provides an estimate of the depth range over which the observed dispersion curve retains meaningful sensitivity to V_s.

S11 Dense DAS imaging reveals localized depth-dependent structure along the Roadside segment

To complement the five discrete profile comparisons, we constructed a pseudo-2D V_s section along the Roadside segment using a denser active-source DAS acquisition (Figure S10b). The same rock-physics framework was then applied to obtain the corresponding pseudo-2D S_w section (Figure S10d). For comparison, the temperature-derived reference profile was extended laterally across the same distance to generate depth-dependent but laterally uniform V_s and S_w baseline models (Figure S10, left).

The reference model shows smooth vertical trends, with V_s increasing and S_w decreasing with depth. In contrast, the DAS-derived pseudo-2D sections show localized deviations from this depth-only pattern. The V_s image contains laterally varying zones of lower and higher velocity, and these spatial variations are expressed in the corresponding S_w section as localized changes in the modeled unfrozen pore water content. Several of these variations extend below the shallow near-surface.

Figure S1. Local acquisition geometry for the five short-offset DAS–geophone comparison sites: (a) Roadside, (b) Tundra 1, (c) Tundra 2, (d) Tundra 3, and (e) Tundra 4. The base map was designed and developed by Esri | Powered by Esri. For more information on this map, visit https://goto.arcgisonline.com/maps/World_Imagery (last access: 13 August 2026).

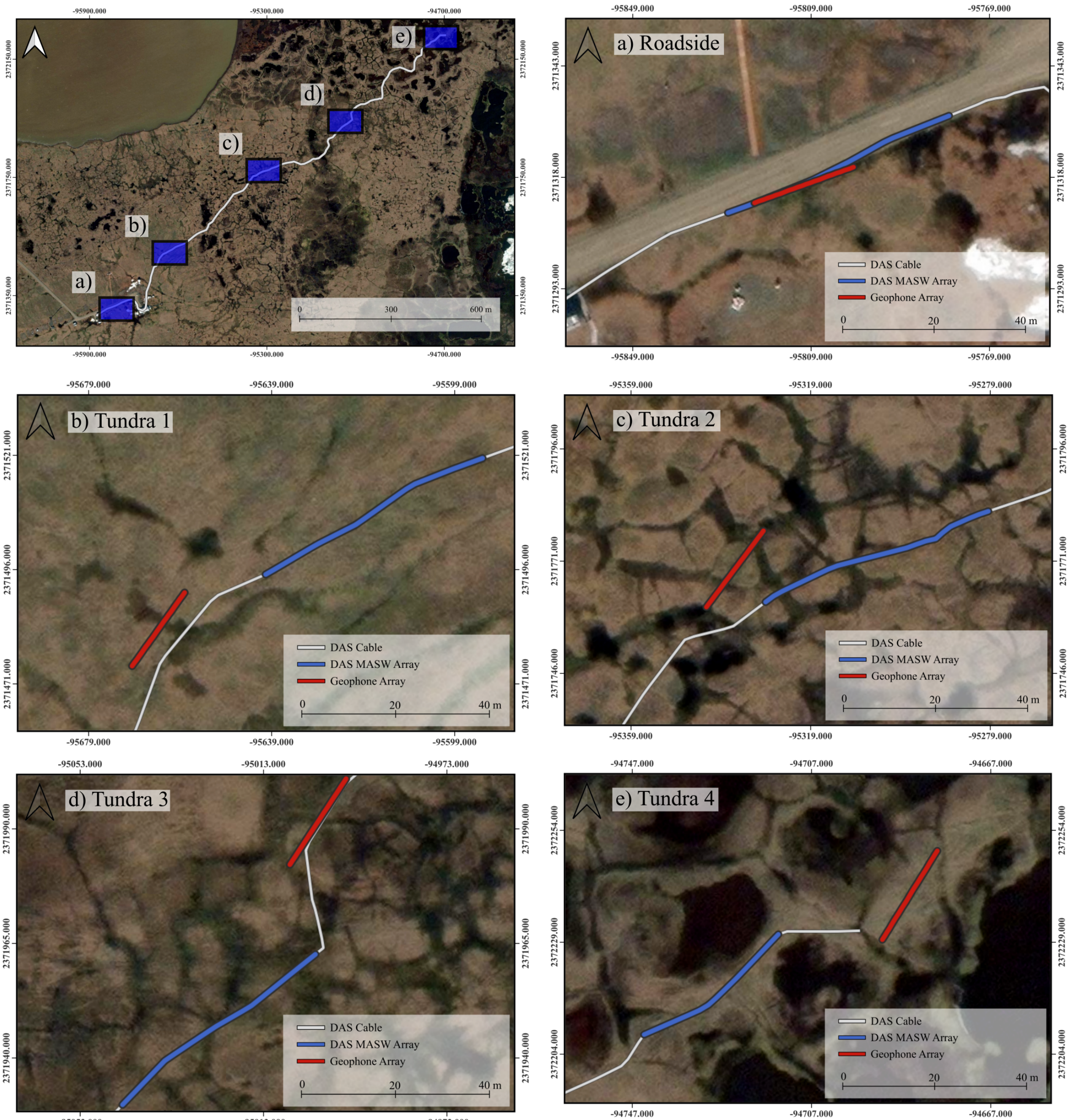

Figure S2. Global porosity reference used in the final V_s–S_w mapping. Thin gray curves show the site-specific porosity profiles obtained from each joint DAS–geophone inversion at the five study locations. The black curve shows the mean porosity profile computed across the five sites. The blue shaded region indicates the p10–p90 range, and the light gray shaded region indicates the full min–max range. This common porosity profile was used to convert the final DAS- and geophone-derived V_s profiles into water saturation estimates.

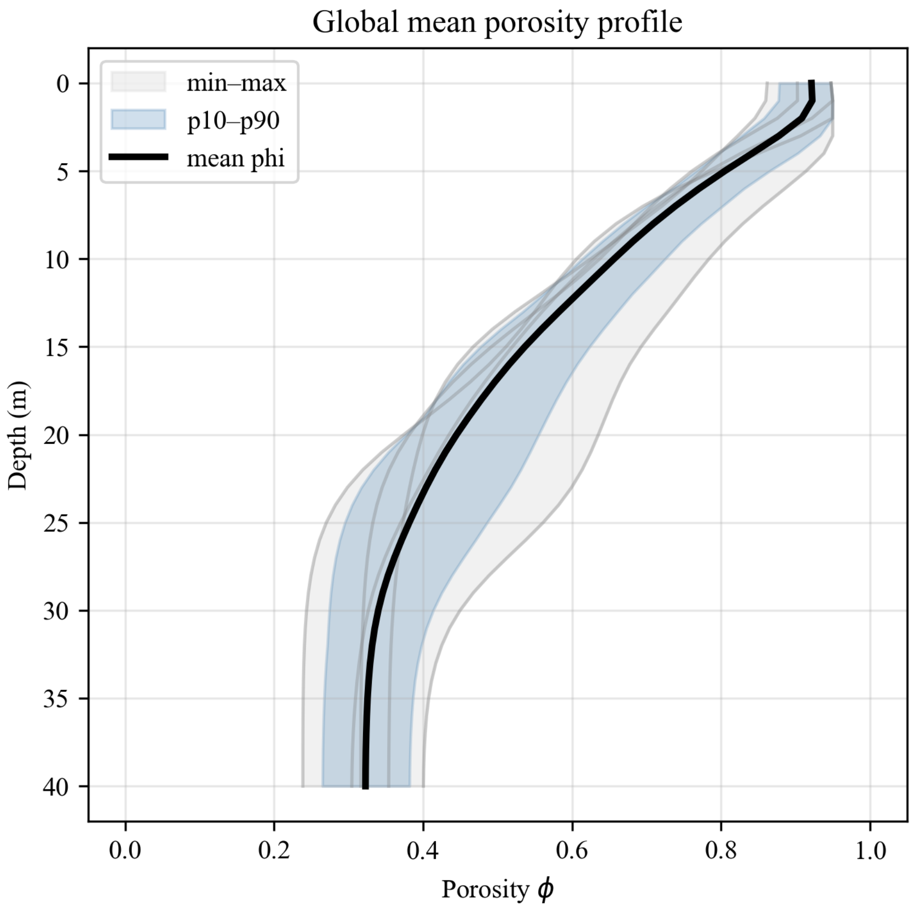

Figure S3. Comparison of five tested V_s-S_w rock-physics models against the temperature- and laboratory-informed reference profile, applied to the median DAS-derived V_s profile at (a) Roadside, (b) Tundra 1, (c) Tundra 2, (d) Tundra 3 and (e) Tundra 4. All models were evaluated using a constant porosity of 0.4, independent of the depth-dependent porosity profile used elsewhere in this study, to isolate differences attributable to the rock-physics formulation itself. The load-bearing model and Carcione (1998) remain closest to the reference across all five sites, while the two-end-member model (Dou et al., 2017), Zimmerman and King (1986), and Minshull (1994) diverge toward implausibly high unfrozen water content ($S_w > 0.6$) by 10–20 m depth. The Carcione (1998) curve additionally predicts $S_w = 0$ at several depths, which we consider inconsistent with the persistence of interfacial liquid water expected at depth.

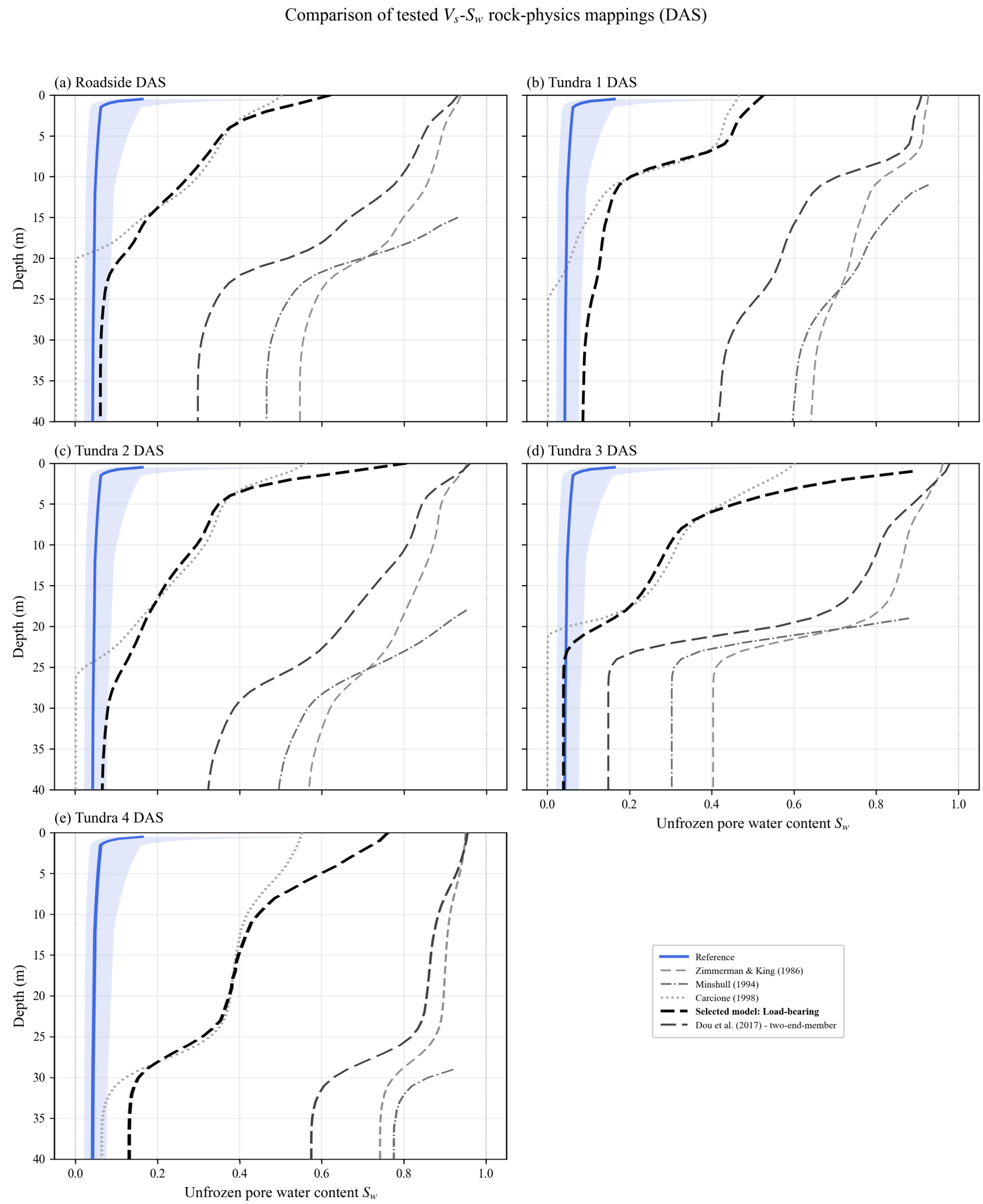

Figure S4. (a) Comparison of the common reference profile (dashed) and site-specific reference profiles (solid) at each of the five sites. Roadside uses the Tundra 1 reference (no local core samples); Tundra 4 has a single core sample, so no envelope is shown. (b) Seismically inferred S_w profiles obtained using the common (faded) and site-specific reference (solid) for geophone (red) and DAS (blue, dashed) at each site.

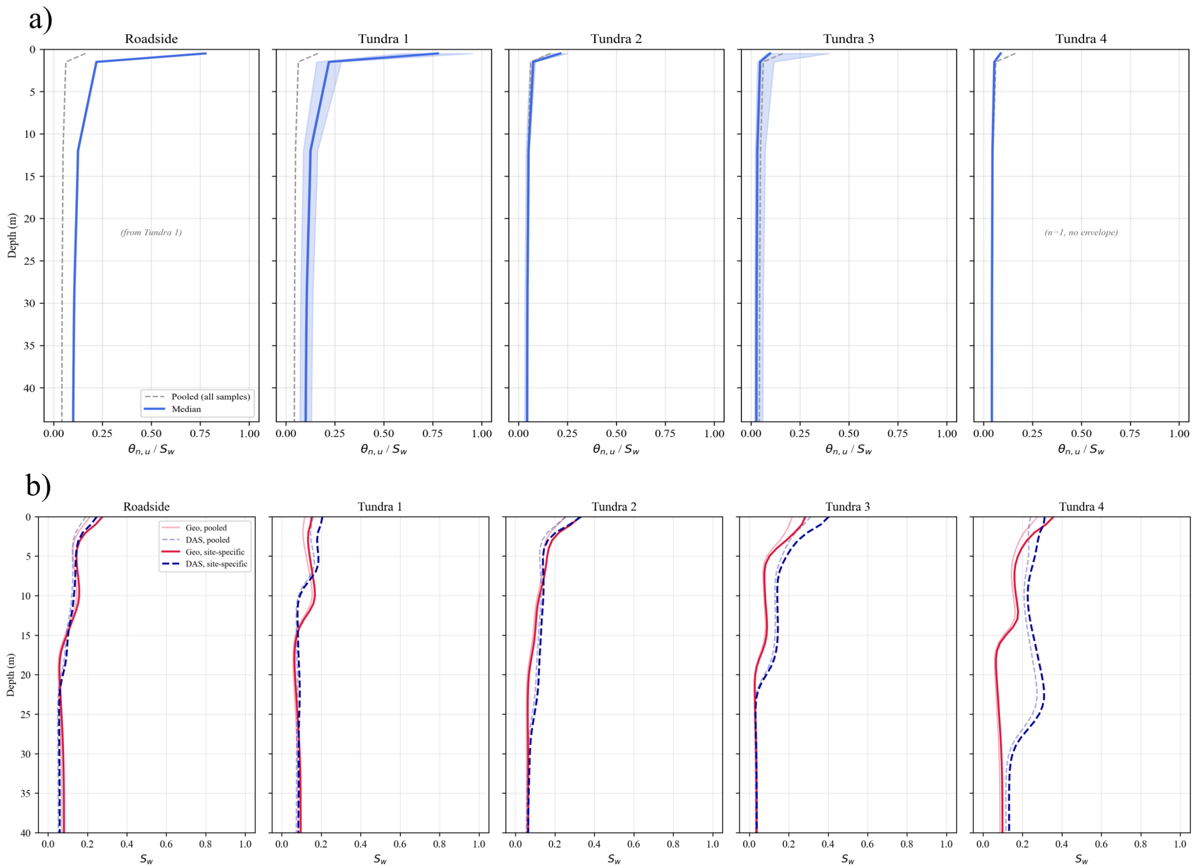

Figure S5. Depth-dependent comparison between DAS and geophone median V_s profiles for sites Roadside, Tundra 1, and Tundra 2. Left: median V_s profiles with uncertainty envelopes (10th–90th percentiles and min–max). Middle: absolute velocity difference and percentage error versus depth. Right: scatter of DAS versus geophone median V_s values with the 1:1 reference line.

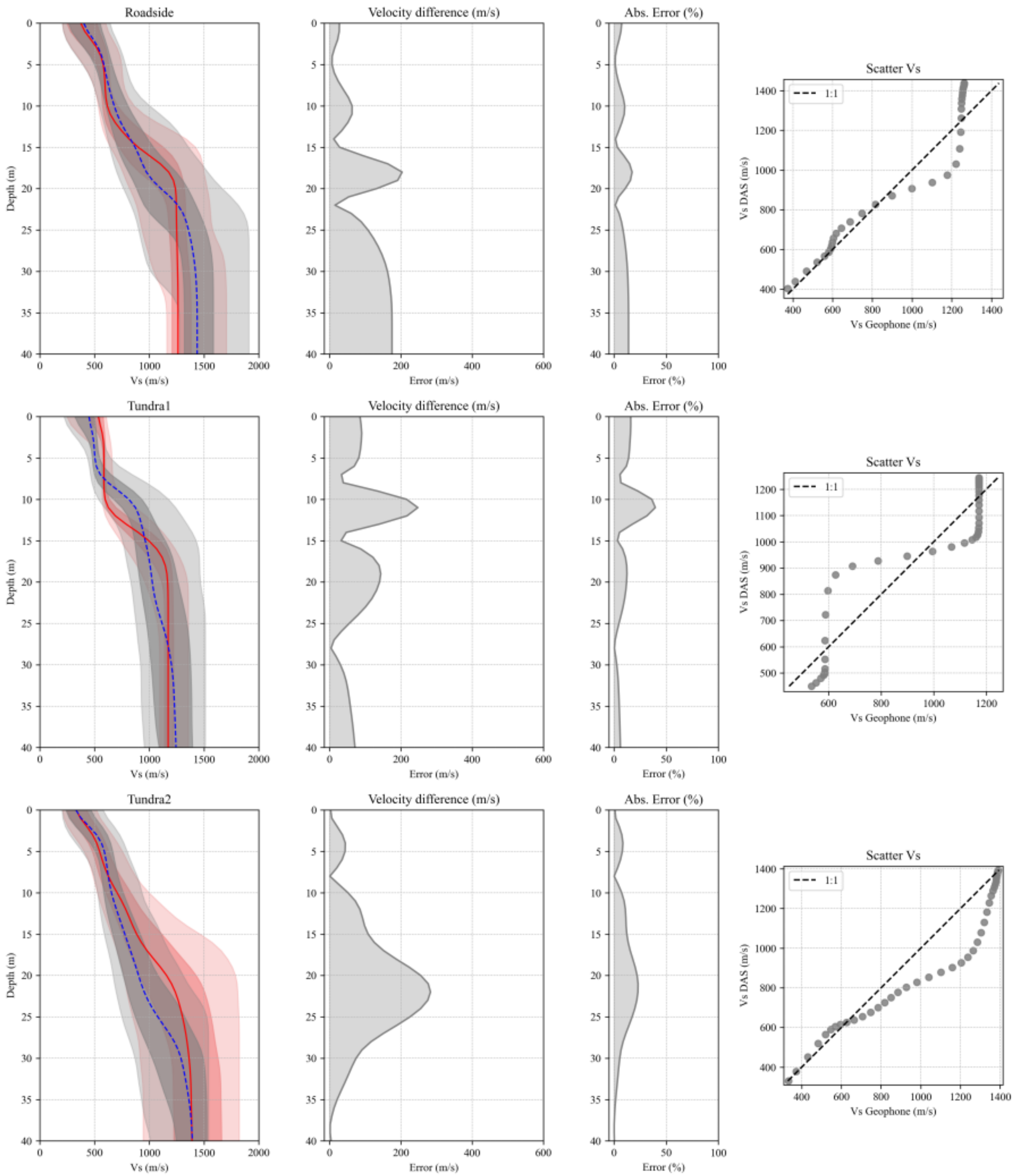

Figure S6. Depth-dependent comparison between DAS and geophone median V_s profiles for sites Tundra 3 and Tundra 4. Left: median V_s profiles with uncertainty envelopes (10th–90th percentiles and min–max). Middle: absolute velocity difference and percentage error versus depth. Right: scatter of DAS versus geophone median V_s values with the 1:1 reference line.

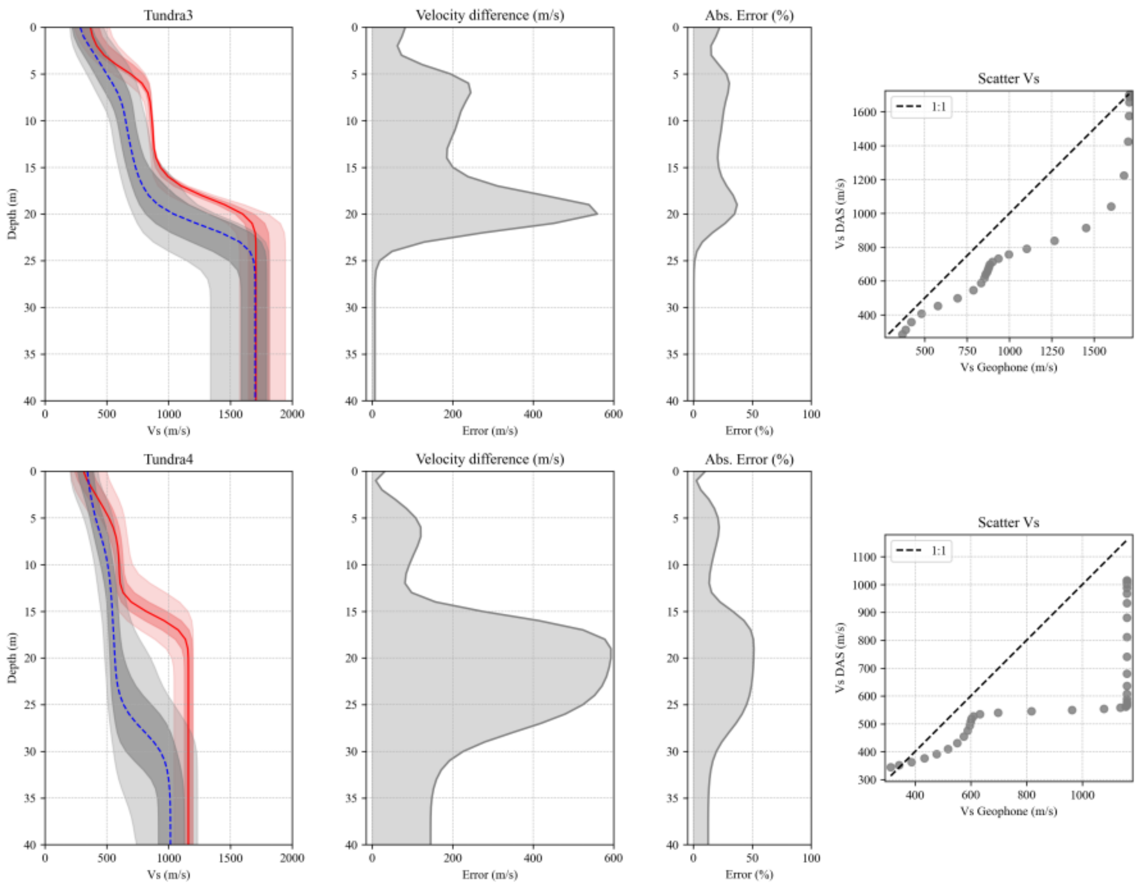

Figure S7. Comparison of dispersion curves derived from the left and right sides of a single DAS shot gather at the Roadside site. Upper part: Shot gathers for the left and right halves of the array, each containing approximately half the total channel range. Lower part: Corresponding frequency–phase velocity dispersion images, with the picked fundamental-mode dispersion curve overlaid. The two sides show measurably different dispersion curves.

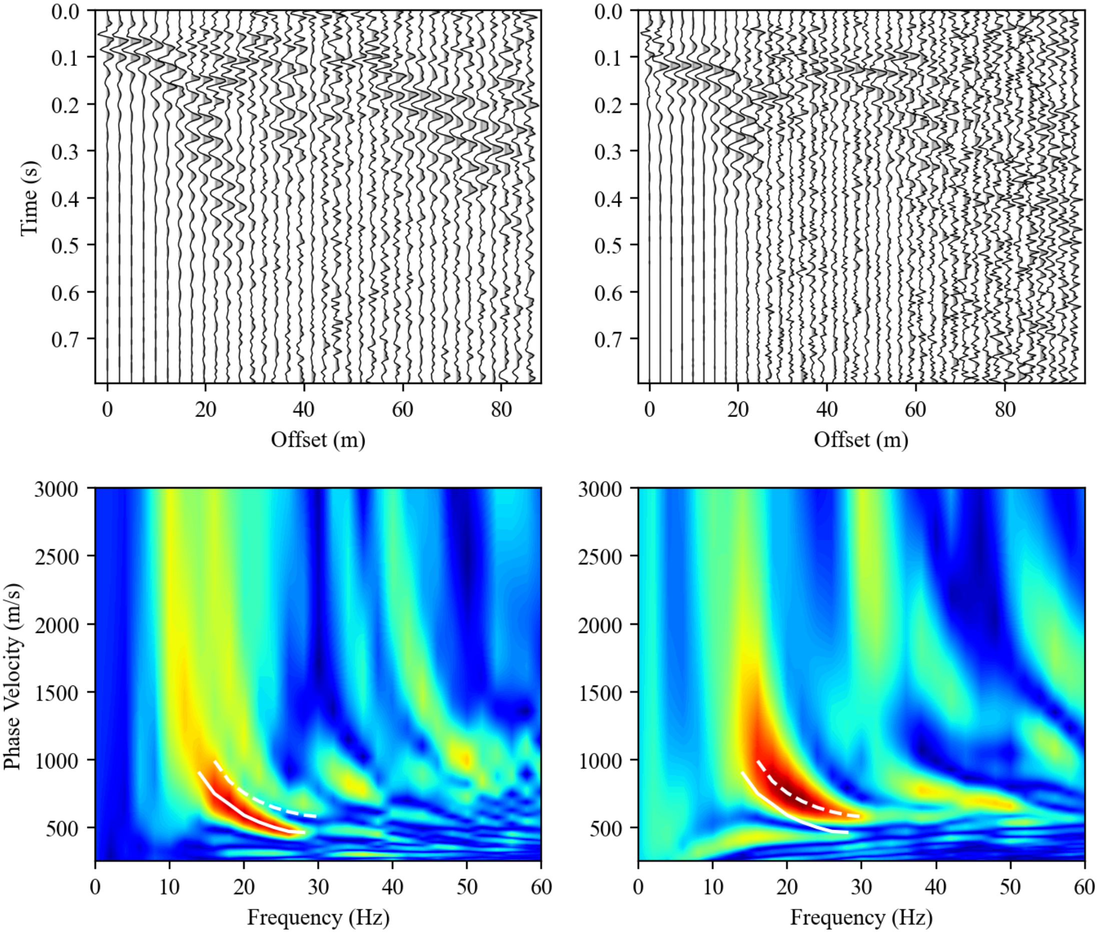

Figure S8. Sensitivity kernels for the fundamental-mode Rayleigh-wave dispersion curves at the five study sites: Roadside, Tundra 1, Tundra 2, Tundra 3, and Tundra 4. For each site, the left panel shows the median V_s profile with uncertainty envelope for geophone (solid red) and DAS (dashed blue); the middle and right panels show the corresponding phase-velocity sensitivity $\partial c/\partial V_s(z)$ as a function of depth and frequency for the geophone and DAS dispersion curves, respectively. Brighter colors indicate greater sensitivity of the observed phase velocity to V_s at that depth and frequency. These kernels were used to estimate the resolution depth reported in Table S8.

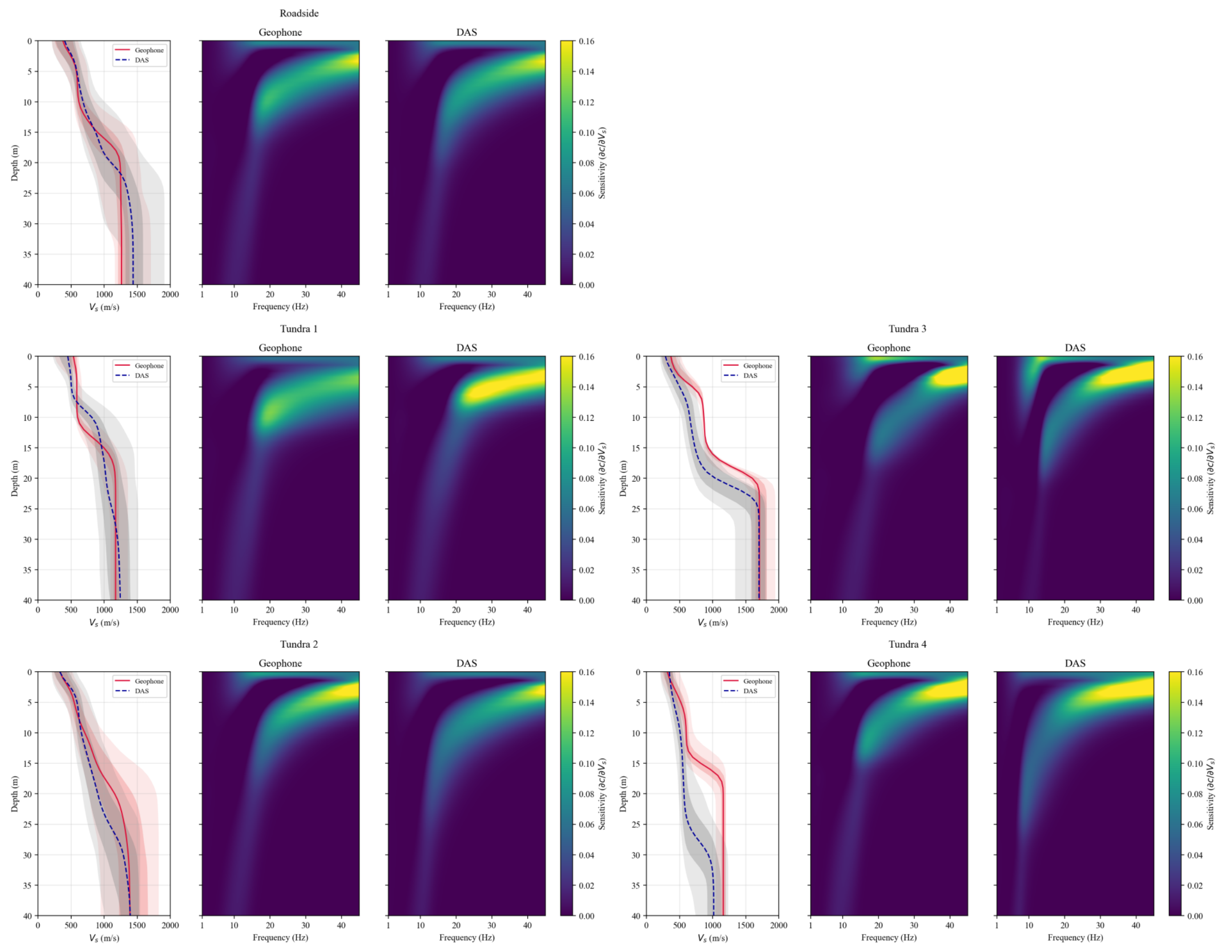

Figure S9. Temperature boreholes used to construct the temperature profile adopted in this study. Gray circles indicate shallow temperature boreholes near the DAS cable, which were used for the upper 0–1.5 m of the profile. The white triangle indicates the deeper temperature borehole used for temperatures below 1.5 m. The base map was designed and developed by Esri | Powered by Esri. For more information on this map, visit https://goto.arcgisonline.com/maps/World_Imagery (last access: 13 August 2026).

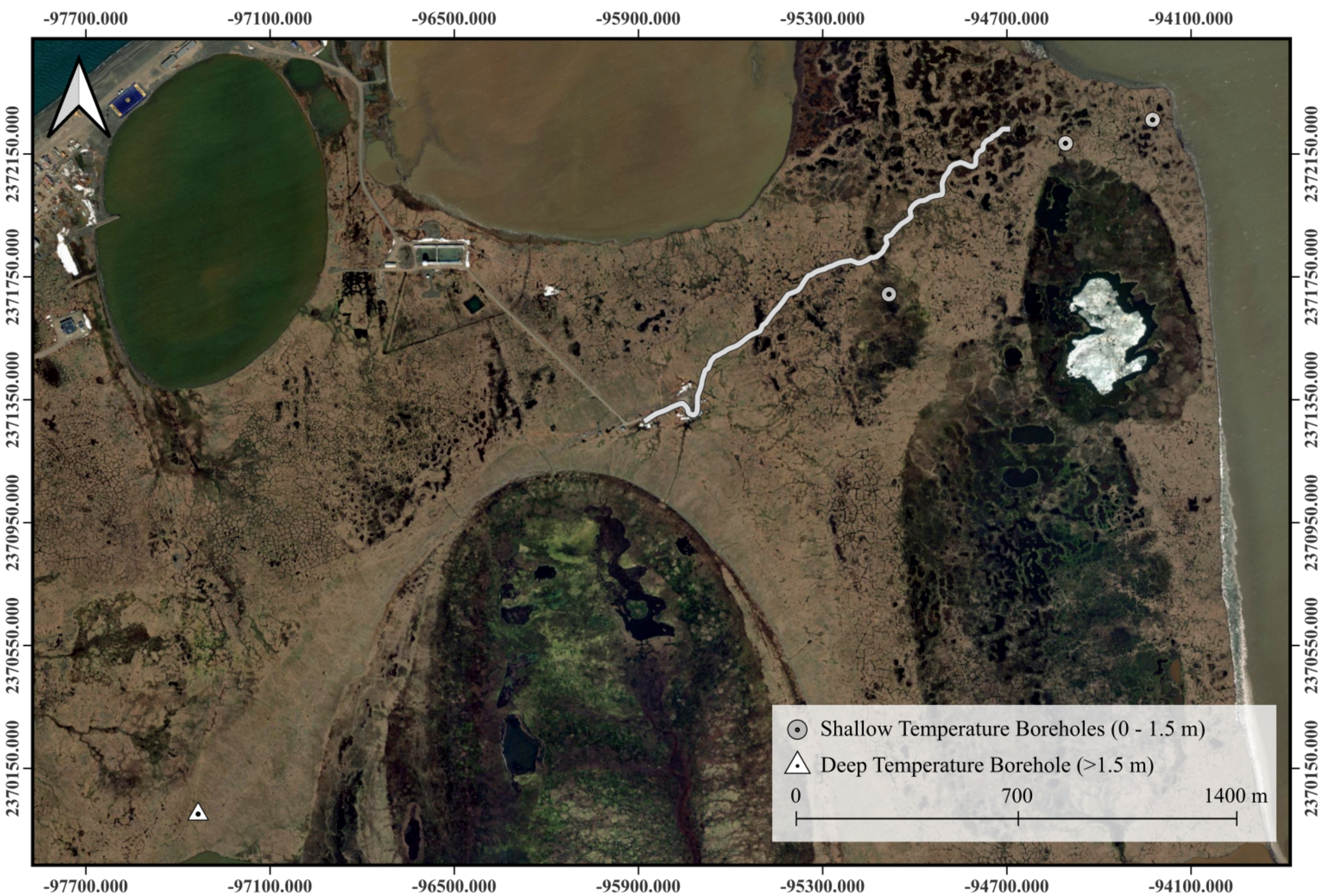

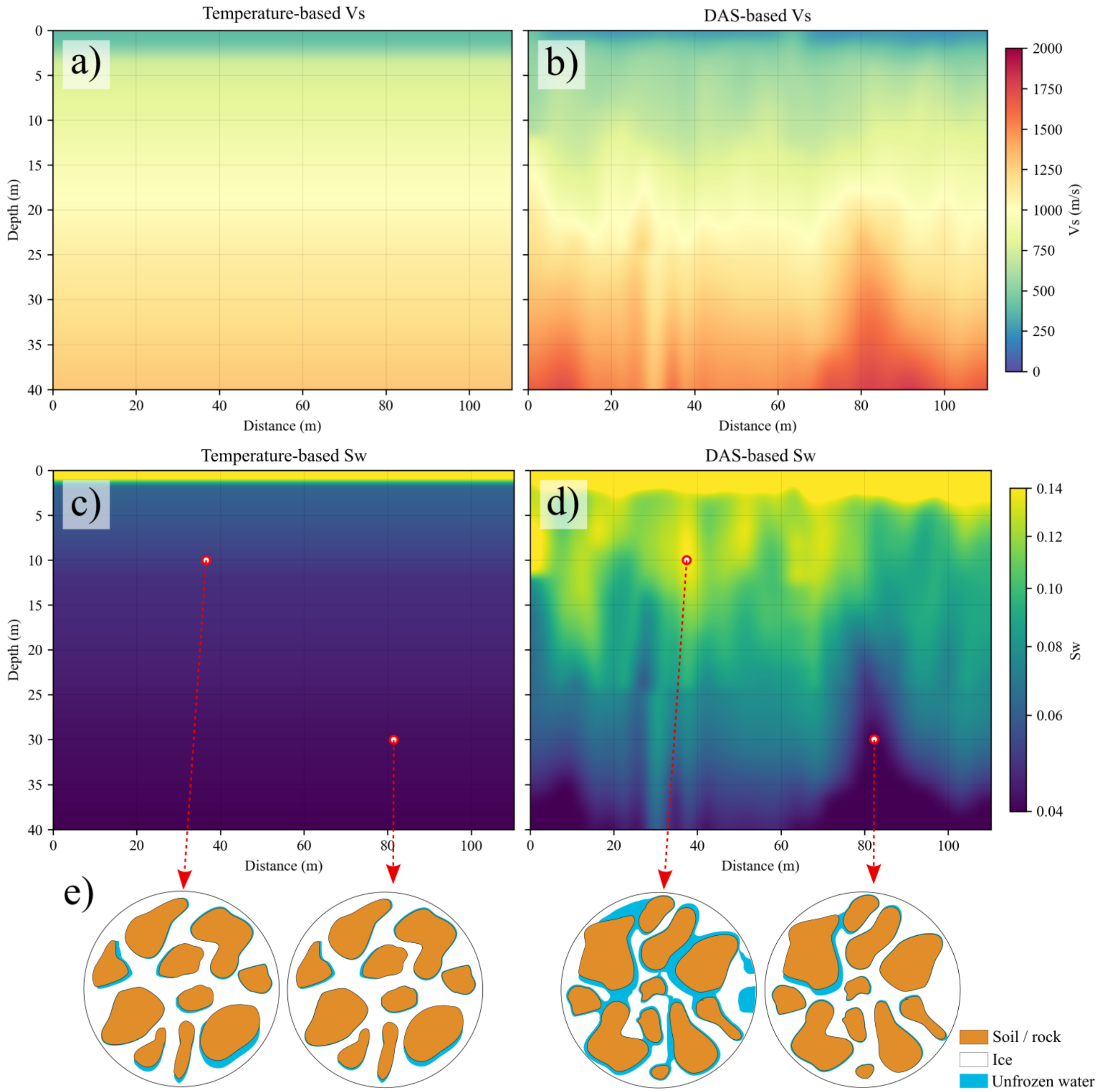

Figure S10. Comparison between a laterally uniform thermal baseline and pseudo-2D DAS-derived sections along the Roadside segment. (a) V_s and (c) S_w baseline models obtained by extending the temperature-derived reference profile laterally across the section. (b) Pseudo-2D V_s section derived from a denser active-source DAS acquisition and (d) corresponding inferred S_w section obtained with the same rock-physics framework. The thermal baseline provides a smooth depth-dependent reference, whereas the DAS-derived sections reveal localized lateral variations that are not represented by a depth-only model. (e) Schematic illustrations to qualitatively represent the interpreted ice–water partitioning under the adopted rock-physics framework.

Table S1. Acquisition, processing, and inversion parameters used for the DAS and geophone MASW analyses.

Parameter	DAS	Geophone
Survey date	August 2024	August 2022
Sampling frequency	1000 Hz	4000 Hz
Channel or receiver spacing	2.45 m	1 m
Gauge length	5 m	–
Downsampled frequency	500 Hz	–
Bandpass filter	0.5–120 Hz	0.5–120 Hz
Pick frequency range	12–50 Hz	8–50 Hz
Maximum inversion depth	40 m	40 m
Number of retained models	1000	1000
V_s bounds	0–2000 m/s	0–2000 m/s

Table S2. Parameters used in the load-bearing rock-physics model (Dou et al., 2017; Dvorkin and Nur, 1996; Helgerud et al., 1999; Mavko et al., 1998; Batzle and Wang, 1992; Woeber et al., 1963; Pounder, 2013).

Parameter	Symbol	Value	Role
Initial porosity	ϕ_0	variable;	
Critical porosity	ϕ_c	0.33	Hertz–Mindlin/HM–HS parameter
Coordination number	n	9.5	grain contact parameter
Effective pressure	P	8.73×10^3 Pa	effective confining pressure
Mineral bulk modulus	K_m	37 GPa	quartz/mineral phase
Mineral shear modulus	G_m	44 GPa	quartz/mineral phase
Mineral density	ρ_m	2650 kg m^{-3}	quartz/mineral phase
Ice bulk modulus	K_i	8.8 GPa	ice phase
Ice shear modulus	G_i	3.5 GPa	ice phase
Ice density	ρ_i	917 kg m^{-3}	ice phase
Water bulk modulus	K_f	2.2 GPa	liquid pore fluid
Water density	ρ_f	1000 kg m^{-3}	liquid pore fluid

Table S3. DAS–geophone contrast in inferred unfrozen pore water content, comparing the common reference and site-specific reference pipelines. The contrast is defined as $\Delta S_w = S_{w,\mathrm{DAS}} - S_{w,\mathrm{Geo}}$, and the table reports the mean absolute difference, mean $|\Delta S_w|$, at each site.

Site	Mean $\lvert\Delta S_w\rvert$ common	Mean $\lvert\Delta S_w\rvert$ site-specific
Roadside	0.0148	0.0168
Tundra 1	0.0209	0.0238
Tundra 2	0.0180	0.0203
Tundra 3	0.0330	0.0376
Tundra 4	0.0900	0.1015

Table S4. Error metrics between DAS and geophone median V_s profiles at each site. Root mean squared difference (RMSD), mean absolute difference (MAD), and mean absolute percentage difference (MAPD) were calculated from the point by point difference between the median V_s profiles over the depth range. Pearson R indicates the linear correlation between each pair of median profiles. The last column shows the lateral distance between the DAS shot location and the selected geophone shot location (the closest geophone shot to the DAS shot at each site).

Site	RMSD (m/s)	MAD (m/s)	MAPD (%)	Pearson R	Distance DAS-Geo (m)
Roadside	119.29	98.78	9.04	0.96	5
Tundra 1	101.03	85.15	10.41	0.93	44
Tundra 2	129.41	94.13	8.91	0.96	25
Tundra 3	207.74	142.38	14.30	0.96	15
Tundra 4	319.45	253.25	25.29	0.76	36

Table S5. Quantitative comparison between the DAS- and geophone-derived S_w profiles. The signed difference is defined as $\Delta S_w = S_{w,\mathrm{DAS}} - S_{w,\mathrm{Geo}}$.

Site	Offset (m)	Mean $\lvert\Delta S_w\rvert$	RMSE ΔS_w	Maximum $\lvert\Delta S_w\rvert$	Depth of maximum contrast (m)	Mean signed ΔS_w
Roadside	5	0.0148	0.0164	0.0285	18	−0.0089
Tundra 1	44	0.0209	0.0277	0.0721	11	0.0015
Tundra 2	25	0.0180	0.0230	0.0454	21	0.0132
Tundra 3	15	0.0330	0.0450	0.0927	0	0.0330
Tundra 4	36	0.0900	0.1112	0.2085	22	0.0879

Table S6. Root-mean-square (RMS) of the reference-relative anomaly $\Delta S_{w,\text{seismic}-\text{ref}} = S_{w,\text{seismic,median}} - S_{w,\text{ref,median}}$ calculated over three depth intervals for the geophone- and DAS-derived profiles at each study site. The full interval covers the modeled depth range up to 40 m. The shallow-to-intermediate (5–20 m) and deep (20–40 m) sub-intervals are reported separately to distinguish anomalies concentrated near the surface from those that persist to greater depth. Larger RMS values indicate a greater model-inferred departure from the temperature- and laboratory-informed reference at that depth range.

	Full Interval		5 - 20 m		20 - 40 m	
Site	Geophone	DAS	Geophone	DAS	Geophone	DAS
Roadside	0.051	0.044	0.065	0.058	0.022	0.009
Tundra 1	0.051	0.052	0.066	0.059	0.033	0.032
Tundra 2	0.050	0.058	0.058	0.071	0.012	0.033
Tundra 3	0.036	0.073	0.025	0.081	0.015	0.014
Tundra 4	0.072	0.160	0.082	0.181	0.035	0.145

Table S7. Resolution-truncated RMS of the reference-relative anomaly $\Delta S_{w,\text{seismic}-\text{ref}} = S_{w,\text{seismic,median}} - S_{w,\text{ref,median}}$. The 0–40 m RMS values correspond to the full modeled interval reported in Table S6. The truncated RMS values were computed from the surface to the resolution depth estimated from the sensitivity kernels. Values reported as > 40 indicate that sensitivity remained above 10% of its peak throughout the modeled 0–40 m interval.

	Resolution depth (m)		RMS 0–40 m		Resolution-truncated RMS	
Site	Geo	DAS	Geo	DAS	Geo	DAS
Roadside	20	30	0.051	0.044	0.068	0.050
Tundra 1	33	27	0.051	0.052	0.053	0.060
Tundra 2	30	> 40	0.050	0.058	0.058	0.058
Tundra 3	26	21	0.036	0.073	0.044	0.099
Tundra 4	23	> 40	0.072	0.160	0.088	0.160

Table S8. Resolution depth estimated from the sensitivity kernel of the fundamental-mode dispersion curve at each site and sensor. $f_{\min}$ is the minimum reliably picked frequency for each dataset. Values reported as > 40 indicate that sensitivity remained above 10% of its peak throughout the modeled 0–40 m interval.

Site	$f_{\min}$ (Hz)		Resolution depth (10% peak, m)	
	DAS	Geo	DAS	Geo
Roadside	16.0	18.4	30	20
Tundra 1	18.4	16.2	27	33
Tundra 2	12.5	15.4	> 40	30
Tundra 3	17.3	15.0	21	26
Tundra 4	15.9	8.2	> 40	23

References

Batzle, M. and Wang, Z.: Seismic properties of pore fluids, Geophysics, 57, 1396–1408, 1992.

Dou, S., Nakagawa, S., Dreger, D., and Ajo-Franklin, J.: An effective-medium model for P-wave velocities of saturated, unconsolidated saline permafrost, Geophysics, 82, EN33–EN50, https://doi.org/10.1190/geo2016-0474.1, 2017.

Dvorkin, J. and Nur, A.: Elasticity of high-porosity sandstones; theory for two North Sea data sets, Geophysics, 61, 1363–1370, https://doi.org/10.1190/1.1444059, 1996.

Helgerud, M. B., Dvorkin, J., Nur, A., Sakai, A., and Collett, T.: Elastic-wave velocity in marine sediments with gas hydrates: Effective medium modeling, Geophysical Research Letters, 26, 2021–2024, https://doi.org/https://doi.org/10.1029/1999GL900421, 1999.

Luu, K.: disba: Numba-accelerated computation of surface wave dispersion, https://doi.org/10.5281/zenodo.5775195, 2021.

Mavko, G., Mukerji, T., and Dvorkin, J.: The rock physics handbook, Cambridge university press, 1998.

Park, C. B., Miller, R. D., and Xia, J.: Imaging dispersion curves of surface waves on multi-channel record, in: SEG Technical Program Expanded Abstracts 1998, pp. 1377–1380, Society of Exploration Geophysicists, 1998.

Park, C. B., Miller, R. D., and Xia, J.: Multichannel analysis of surface waves, Geophysics, 64, 800–808, 1999.

Pounder, E. R.: The physics of ice, Elsevier, 2013.

Wang, Z., Xiao, M., Bray, M., Nicolsky, D., and Ji, X.: Creep Deformation and Long-Term Strength of Ice-Rich Permafrost in Northern Alaska, Journal of Geotechnical and Geoenvironmental Engineering, 152, 04025 161, https://doi.org/10.1061/JGGEFK.GTENG-13324, 2025.

Woeber, A., Katz, S., and Ahrens, T.: Elasticity of selected rocks and minerals, Geophysics, 28, 658–663, 1963.